

Preparation of WO₃ Nanoplate for Photocatalytic Degradation of Rhodamine B

¹Xiaoyuan Zhang, ²Wenbin Hu, ¹Yaping Chen, ¹Jinhua Xiong*

¹Fujian Provincial Key Laboratory of Clean Energy Materials, Longyan University, Longyan 364000, China.

²Department of Chemical Engineering, Fuzhou University Zhicheng College, Fuzhou 350002, China.

jhxiong@lyun.edu.cn*

(Received on 8th May 2024, accepted in revised form 23rd August 2024)

Summary: Herein, WO₃ nanoplate was synthesized via a top-down route. A single crystal with monoclinic structure of WO₃ nanoplate was confirmed by X-ray diffraction (XRD) and transmission electron microscopy (TEM). The activity of photocatalytic degradation Rhodamine B (RhB) over the WO₃ nanoplate increased by about 1.4 times, when compared with that of bulk WO₃. The enhancement of activity was attributed to the unique two-dimension (2D) structure leading to an effective separation of carriers, which was further verified via steady and time-solution fluorescence spectra (PL), photocurrent and electrochemical impedance spectra (EIS).

Key words: WO₃ nanoplate, Carriers separation, Photocatalysis, Degradation, Top-down

Introduction

With the development of society, energy and environment issues have become the main factors impacting sustainable development of human beings [1]. Photocatalysis is a technology that semiconductor materials under excited by solar energy produce photogenerated carriers to directly or indirectly trigger chemical redox reactions, which has been regarded as an emerging technology for solving energy and environmental problems [2, 3].

Among many photocatalysts, WO₃ shows a promising application in organic pollutants degradation because of its suitable energy band structure, non-toxicity, stability, et al [4, 5]. Generally, WO₃ has a band-gap of 2.6 eV with a conduction and valence band edge locating at 0.2 eV and 2.8 eV (vs. NHE, pH=0), respectively, which endows WO₃ with an excellent photocatalytic degradation performance under visible light. While, bulk WO₃ photocatalysts are limited by carriers separation efficiency, poor active sites and small specific surface area. In view of these drawbacks of bulk WO₃, regulating the structure of WO₃ via crystal engineering has been considered as a facile way to improve its photocatalytic performance.

As well known, photocatalytic reaction generally includes three main processes: (1) the semiconductor material generates photo-generated charge carriers under photo-excitation; (2) photogenerated carriers are effectively separated and transferred to the active site on the surface of the

materials; (3) Under the allowance of thermodynamic conditions, photogenerated carriers undergo desirable redox reactions on the catalyst surface [6]. An ideal photocatalyst is one in which the surface and interior of the crystal are free of defects, the recombination of the photogenerated carriers can be effectively inhibited and a very short distance needs to be transported before participating the surface catalytic reaction. Hence, constructing nanocrystals into ultrathin nanosheets with two-dimensional (2D) structures can achieve rapid carrier separation and greatly shorten the migration distance [7, 8]. Unique two-dimensional plate structure can be modified or grafted various photocatalytic cocatalysts to promote catalytic reaction kinetics [9]. Thus, two-dimensional semiconductor are very promising materials for improving the quantum efficiency of photocatalysis [10].

Herein, two-dimensional (2D) WO₃ nanoplate was synthesized through a top-down approach. Compared with B-WO₃, WO₃ nanoplate showed an enhanced RhB degradation activity, about 2.4 times of B-WO₃. The enhanced photocatalytic activity of WO₃ nanoplate was attributed to the repression of photo-generated carriers recombination, which was further verified via steady and time-solution PL spectra, photocurrent and EIS spectra. This work will show a positive effect of the 2D WO₃ nanoplate on the photocatalytic performance due to an enhanced carrier separation efficacy and increasing

*To whom all correspondence should be addressed.

surface active sites. We believe the present work will shed lights on the research of 2D nanosheets for photocatalysis.

Experimental

Materials

All the analytical grade materials were purchased from Sinopharm Chemical Reagent Co. and used directly. Octylamine (C_8N), heptane (C_7), tungsten trioxide (WO_3), bismuth trioxide (Bi_2O_3), hydrochloric acid (HCl, 36-38 wt.%), nitric acid (HNO_3 , 65-68 wt.%), rhodamine b (RhB), home-made deionized water.

Preparation details for photocatalysts

$Bi_2W_2O_9$ was synthesized by calcinations of stoichiometric mixtures of tungsten trioxide (WO_3) and bismuth trioxide (Bi_2O_3) at 800 °C for 20 h with a heating rate of 3 °C/min. $H_2W_2O_7$ was obtained by etching of $Bi_2W_2O_9$ with HCl (6 M), refreshing every 2 days for 3 times. Then, $H_2W_2O_7$ sample was obtained by centrifugation and washed with deionized water until pH=7. Inorganic-organic hybrid of C_8N^+/W_2O_7 was prepared via dispersion of 4 g $H_2W_2O_7$ into the mixture solution of C_8N (33 mL) and C_7 (165 mL). After stirring for 3 days, C_8N^+/W_2O_7 was obtained by centrifugation, washing with C_7 and drying at 60 °C in a vacuum oven [11]. H_2WO_4 was prepared via etching of C_8N^+/W_2O_7 by using 7 M HNO_3 for 3 days and then washing with deionized water. WO_3 nanoplate was prepared via calcination of H_2WO_4 at 450 °C for 2 h under air condition [12, 13]. Bulk WO_3 (B- WO_3) was obtained via calcination of $H_2W_2O_7$ at 450 °C for 2 h under air condition.

Characterization

The structures of the as-prepared samples were analysed by X-ray diffractometer (XRD, Bruker D8 Advance with Cu K α radiation). The morphologies were observed via Field-emission scanning electron microscopy (FESEM, Hitachi SU8000 and S4800) and Transmission electron microscopy images (TEM, FEI Tecnai 20). Valence band X-ray photoelectron spectroscopy (XPS) was used to Figure out the energy band position of the samples, which was performed on a ThermoFischer system with a monochromatic Al K α source. $C_{1s}=284.8$ eV was used as the reference date for calibration. To analyse the optical absorption properties of samples, UV-vis absorption spectra (UV-vis abs) were collected via a UV-vis spectrophotometer (Varian Cary 500).

For unravelling the carrier dynamics, photocurrent response and electrochemical impedance spectroscopy (EIS) were performed on CHI660E electrochemical work station with a conventional three-electrode electrochemical cell. A home-made FTO electrode, platinum foil and Ag/AgCl electrode were used as the working electrode, counter electrode and reference electrode, respectively. The electrolyte was 0.2 M Na_2SO_4 aqueous solution. Photocurrent tests were carried out under A 300 W Xenon lamp as the light source. EIS experiments were carried out under a bias voltage of 5 mV with frequencies ranging from 4 MHz to 0.1 Hz. The working electrodes were prepared via dropping the samples onto the conductive fluorine-doped tin oxide glass. Typically, 8 mg sample was well dispersed in 0.5 mL N,N-dimethylformamide via ultrasound and then 15 μ L sample was dropped on the clean FTO with a 0.25 cm². The work electrode was dried at 120 °C for 2 h before use. A fluorescence spectrometer (Edinburgh FLS1000) was used for steady-state and time-resolution photoluminescence (PL) tests under the 397 nm laser as exciting light. The average lifetime of carriers was evaluated by the equation of $\tau = \tau_1 * Rel_1\% + \tau_2 * Rel_2\%$. A TriStar II Plus apparatus (Micromeritics Instrument Corp) was used for testing the N_2 adsorption Brunauer-Emmett-Teller (BET) surface areas and pore distribution curves. Micro-confocal Raman spectroscopy (Renishaw Co.) was carried out at room temperature using the 532 nm laser, for investigating the structure of the samples.

Photocatalytic tests

In a 100 mL bottle, 50 mg photocatalyst was dispersed well in 40 mL RhB aqueous solution (20 ppm) with ultrasound. Before photocatalytic reaction, an adsorption-desorption equilibrium was established via stirring the mixture solution in the dark for 30 min. For photocatalytic reaction, the dispersion solution was irradiated with a xenon light. Along with the progress of the reaction, 1.5 mL of the suspension was taken out and centrifuged for analysis via UV-vis spectrophotometer at certain intervals [14].

Results and Discussion

Structures and Morphologies

Fig. 1A-B showed the XRD diffraction dates for each intermediate product during sample

preparation. Fig. 1A demonstrated the diffraction peaks of the as-prepared $\text{Bi}_2\text{W}_2\text{O}_9$ matched well with the reported data (PDF#33-0221), indicating that high-quality $\text{Bi}_2\text{W}_2\text{O}_9$ was obtained. After corrosion by hydrochloric acid, $\text{Bi}_2\text{W}_2\text{O}_9$ was transformed into $\text{H}_2\text{W}_2\text{O}_7 \cdot n\text{H}_2\text{O}$ ($\text{H}_2\text{W}_2\text{O}_7\text{-air}$) due to the replacement of $\text{Bi}_2\text{O}_2^{2+}$ layer by H_3O^+ [11, 15]. While, the interlayer H_2O of $\text{H}_2\text{W}_2\text{O}_7 \cdot n\text{H}_2\text{O}$ was able to be removed via heat-treatment of $\text{H}_2\text{W}_2\text{O}_7 \cdot n\text{H}_2\text{O}$ under 80°C ($\text{H}_2\text{W}_2\text{O}_7\text{-}80^\circ\text{C}$). As shown, compared with $\text{H}_2\text{W}_2\text{O}_7\text{-air}$, the XRD diffraction peaks of $\text{H}_2\text{W}_2\text{O}_7\text{-}80^\circ\text{C}$ shifted to higher diffraction angles, because the loss of interlayer H_2O lead to a smaller interlayer spacing [13]. Furthermore, the (00 l) ($l=2, 4, 6$) diffraction peaks of $\text{H}_2\text{W}_2\text{O}_7$ shifted to lower angles with the insertion of octylamine into interlayers of $\text{H}_2\text{W}_2\text{O}_7$, which resulted in the formation of organic-inorganic hybrid ($\text{C}_8\text{N}^+/\text{W}_2\text{O}_7$) [16]. Moreover, H_2WO_4 formed after $\text{C}_8\text{N}^+/\text{W}_2\text{O}_7$ hybrid was etched by HNO_3 . As shown, the XRD diffraction patterns of H_2WO_4 was coincident with the reference (PDF#43-0679). Finally, after calcination of H_2WO_4 at 450°C for 2 h, WO_3 nanoplates were obtained. XRD diffraction patterns in Fig. 1B of both WO_3 nanoplate and Bulk WO_3 matched well with that of monoclinic WO_3 (PDF#43-1035) [17]. However, compared with bulk WO_3 , WO_3 nanoplate had a lower XRD diffraction peak strength of (002), meaning a relative poor crystallinity in [002] direction. As well known, the [002] direction was the stacking direction of W-O layer for both $\text{H}_2\text{W}_2\text{O}_7$ and H_2WO_4 . Since WO_3 nanoplate and bulk WO_3 were obtained via interlayer dehydration of H_2WO_4 and $\text{H}_2\text{W}_2\text{O}_7$ respectively, a lower diffraction peak intensity of (002) meant a thinner layer. Additionally, Raman spectra have been widely used in the structural

analysis of materials. Fig. 1C showed bulk WO_3 and WO_3 nanoplate had same Raman spectra, but Raman peak strength of WO_3 nanoplate was weaker than that of bulk WO_3 , indicating WO_3 nanoplate had the same structure with bulk WO_3 , but a relatively poor crystallinity, which corresponded to the XRD analysis results [7]. The three major Raman peaks at 270, 715 and 805 cm^{-1} were attributed to O-W-O bending vibration and W-O-W stretching vibration of monoclinic WO_3 , respectively [18, 19].

For observation the morphologies of the samples, scanning electron microscopy and transmission electron microscopy were used. As shown in Fig. 2, $\text{Bi}_2\text{W}_2\text{O}_9$ was a kind of blocky materials. $\text{H}_2\text{W}_2\text{O}_7$ had an obvious layered structure resulted from the elimination of $\text{Bi}_2\text{O}_2^{2+}$ layer in $\text{Bi}_2\text{W}_2\text{O}_9$ by HCl corrosion. $\text{C}_8\text{N}^+/\text{W}_2\text{O}_7$ hybrid had a fibrous-like morphology due to the curling of $\text{W}_2\text{O}_7^{2-}$ layer caused by the insertion of octylamine [20]. H_2WO_4 presented a nanoplate-like morphology, because organic matter in the $\text{C}_8\text{N}^+/\text{W}_2\text{O}_7$ hybrid was removed under strong acid condition, and W-O layer was rearranged to form H_2WO_4 nanoplate. Bulk WO_3 and WO_3 nanoplate both maintained the morphology of their precursor, displaying a blocky and nanoplate-like morphology, respectively. TEM was further used for confirming the morphology and crystal structure of WO_3 nanoplate (Fig. 3A). As shown, WO_3 nanoplate with different sizes stacked together, and the high-resolution transmission electron microscopy (HRTEM) image (Fig. 3B) showed WO_3 nanoplate had distinct lattice fringes with spacing of 0.364 nm and 0.373 nm, corresponding to the (200) and (020) crystal faces of monoclinic WO_3 , respectively [21].

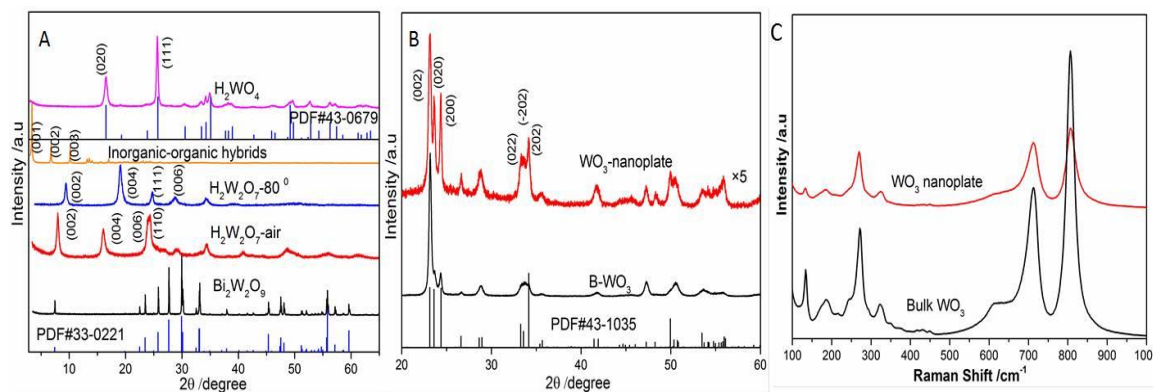


Fig. 1: A-B) the XRD diffraction patterns of the as-prepared samples, C) the Raman spectra of WO_3 nanoplate and bulk WO_3 .

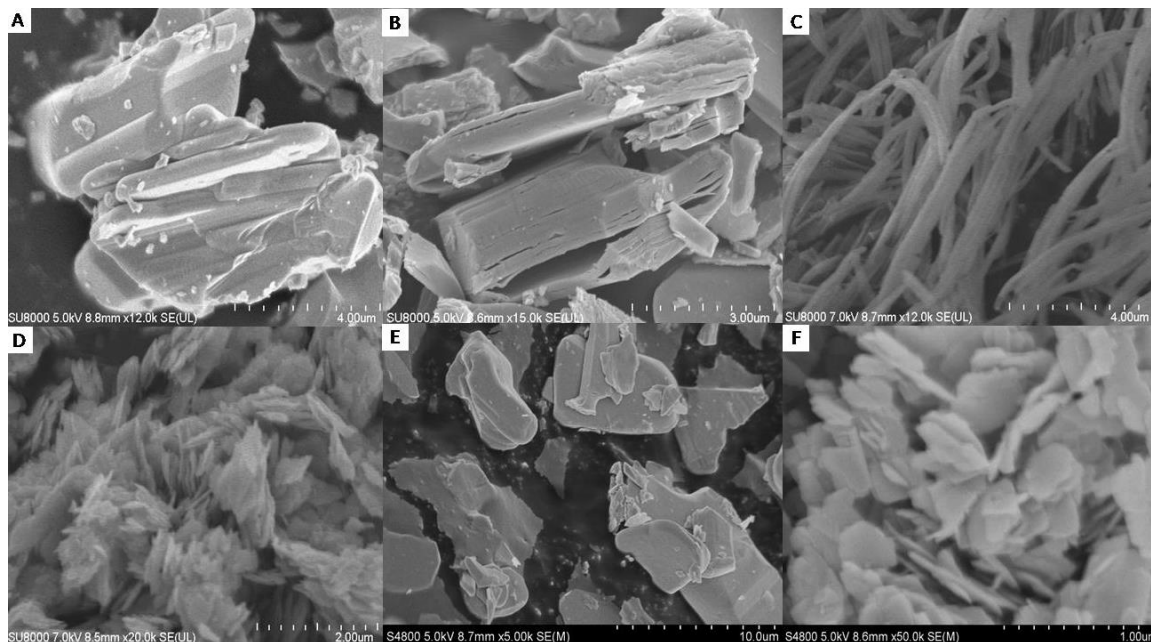


Fig. 2: SEM images of A) Bi₂W₂O₉, B) H₂W₂O₇, C) C₈N⁺/W₂O₇, D) H₂WO₄, E) bulk WO₃ and F) WO₃ nanoplate.

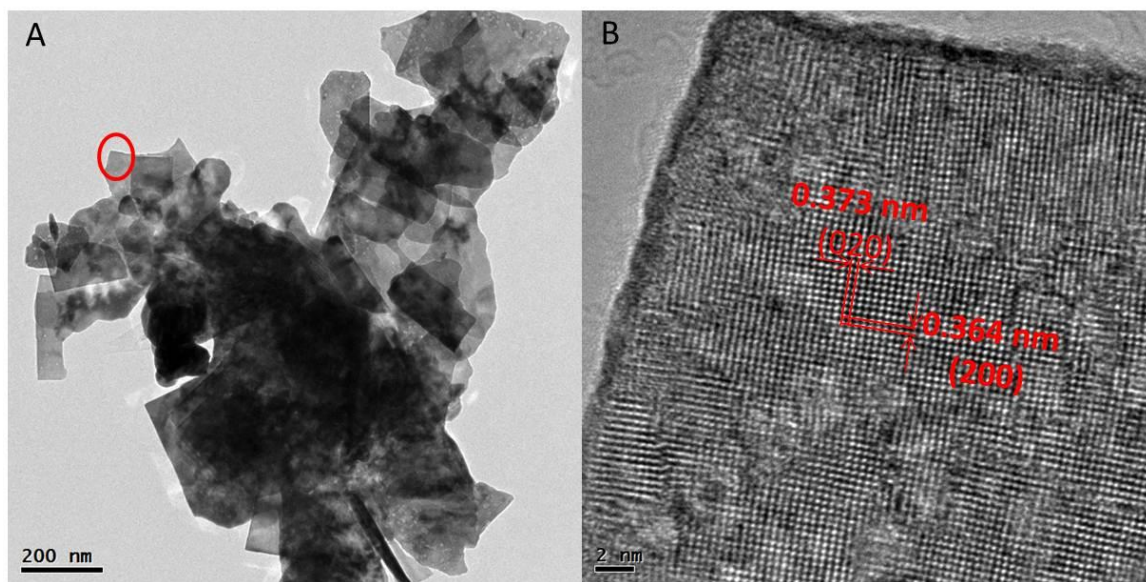


Fig. 3 A) TEM and B) HRTEM images of WO₃ nanoplate

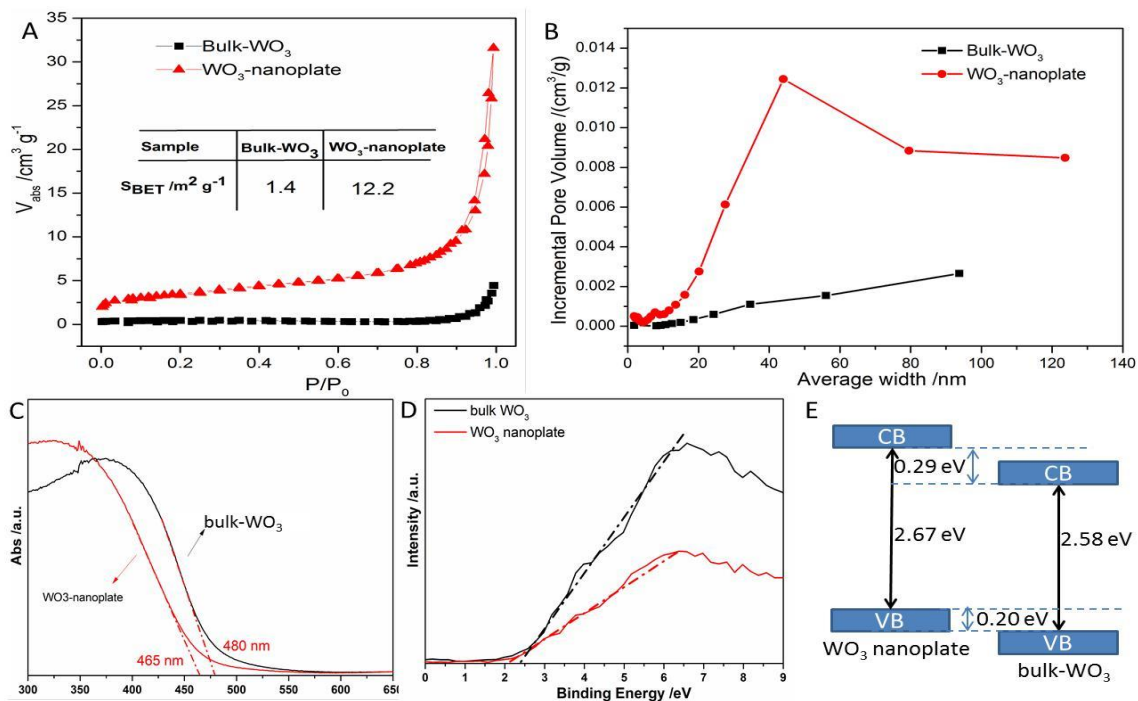


Fig. 4: A) BET absorption at different P/P_0 , B) Pore size distribution curves, C) Uv-vis absorption spectra, D) Valence band XPS spectra, and E) Energy band alignments for WO₃ nanoplate and bulk WO₃.

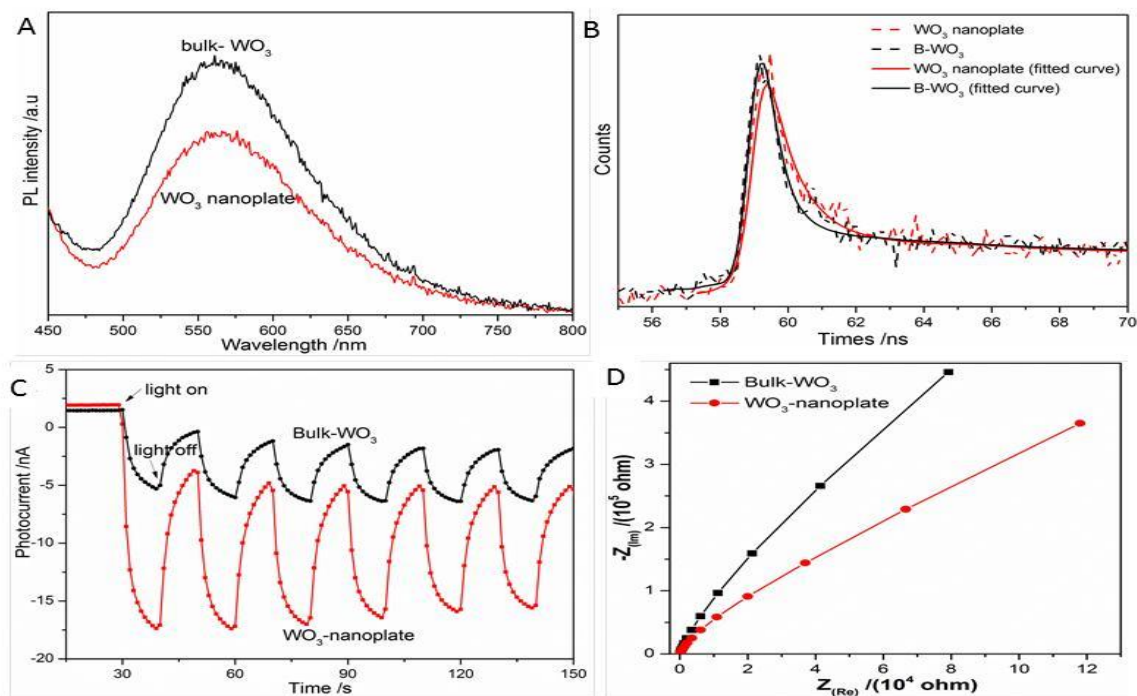


Fig. 5: A) PL spectra and B) PL decay spectra excited by 397 nm laser, C) Photocurrent response curve, D) Electrochemical impedance spectra for WO₃ nanoplate and bulk WO₃.

Surface areas, optical absorption properties and charge Separation.

Fig. 4A showed the N₂ adsorption-desorption curve of the samples. The specific surface areas of B-WO₃ and WO₃ nanoplate were 1.4 m²g⁻¹ and 12.2 m²g⁻¹ respectively, indicating that the 2D planar structure of the WO₃ nanoplate effectively increased the specific surface area. Generally, photocatalysts with large specific surface area could provide more reactive sites, thus enhancing the photocatalytic reaction activity. The pore size distribution curves in Fig. 4B demonstrated B-WO₃ had no obvious pores, while WO₃ nanoplate exhibited pores with average size about 50 nm. The pores in WO₃ nanoplate existed among the restacked WO₃ nanoplates. Additionally, UV-vis absorption spectra in Fig. 4C showed bulk B-WO₃ and WO₃ nanoplate respectively had absorption edges (λ_{abs}) at about 480 and 465 nm. Compared with B-WO₃, a blue shift of 15 nm of the λ_{abs} of WO₃ nanoplate was ascribed to the quantum size effect [21]. Additionally, based on empirical formula of $E_g = 1240/\lambda_{\text{abs}}$ (E_g is bandgap), the E_g of B-WO₃ and WO₃ nanoplate were 2.58 and 2.67 eV, respectively [22]. Additionally, valence band X-ray photoelectron spectroscopy (XPS) in Fig. 4D further revealed the ΔE between the valence band maximum (E_{vb}) and Fermi level (E_{F}) were around 2.18 eV for WO₃ nanoplate and 2.38 eV for bulk WO₃. Based on the differences in E_g and E_{VB} between WO₃ nanoplate and B-WO₃, their band alignments were given in Fig. 4E. Furthermore, the conduction band (E_{cb}) and E_{vb} were -0.79 and 1.88 V for WO₃ nanoplate, -0.50 and 2.08 V for bulk WO₃ respectively, due to $E_{\text{cb}} = E_{\text{vb}} - E_g$ and $E_{\text{vb}} = \Delta E + \Phi - E_{\text{vac}}$. E_{vac} and work function Φ were 4.5 and 4.2 eV, respectively.

Fluorescence technique (PL) is an effective method to study the photo-generated carrier separation efficiency. Usually, after the semiconductor is excited, the recombination of photo-generated carriers will be manifested in the form of fluorescence. A stronger intensity of fluorescence indicates a higher recombination rate [23]. Fig. 5A showed the PL intensity of WO₃ nanoplate was weaker than that of B-WO₃, indicating WO₃ nanoplate had a more efficient separation [24]. Additionally, the decay PL spectra displayed in Fig. 5B further verified the photo-induced carriers of WO₃ nanoplate had a more prolonged average lifetime than bulk WO₃, 9.7 and 20.1 ns for B-WO₃ and WO₃ nanoplate respectively. The increased carriers lifetime was of importance for promoting photo-induced carriers taking part in photocatalytic redox reaction before recombination [25]. Furthermore, the photocurrent response (Fig. 5C) and electrochemical impedance spectroscopy (Fig. 5D) demonstrated WO₃ nanoplate had an enhanced photocurrent and a lower impedance compared with B-WO₃, further verifying WO₃ nanoplate had a more rapid separation

efficiency and charge mobility of photogenerated carriers [26, 27]. Therefore, it was inferred that the unique two-dimensional structure of WO₃ nanoplate could effectively accelerate the separation and migration of photo-induced carriers, which predicted WO₃ nanoplate would have a better photocatalytic activity than B-WO₃.

Photocatalytic activity

The photocatalytic degradation of RhB was used to investigate the photocatalytic performance of WO₃ nanoplate and bulk WO₃. Fig. 6A exhibited the changes of the absorption spectra of RhB along with the photocatalytic reaction process over WO₃ nanoplate. Additionally, the RhB solution after photocatalytic reaction was colorless (inset in Fig. 6A). As reported, if the characteristic absorption of RhB solution in Uv-vis absorption spectra decreased to about zero directly without a significant shift, it demonstrated degradation of RhB suffered from mineralization via cleavage of the whole conjugated chromophore structure of RhB [28-30]. Fig. 6B demonstrated the degradation rate of RhB reached 96 % after 6 h illumination, while only about 40 % was degraded over B-WO₃ under the same conditions. Considering that the adsorption quantities over B-WO₃ and WO₃ nanoplate after adsorption-desorption equilibrium in dark were both only about 5% (Fig. 6C), and trace degradation for RhB solution without catalyst, the decreases in RhB concentration over B-WO₃ and WO₃ nanoplate were certainly ascribed to photocatalysis. Obviously, the photocatalytic activity of WO₃ nanoplate was higher than that of B-WO₃, which arose from the more rapid separation efficiency and charge mobility of photogenerated carriers over WO₃ nanoplate. Furthermore, according to the literature, at pH=7, the potential for oxygen to be reduced to superoxide radical was -0.28 eV (O₂/O₂^{-•}), and the potential for water molecules to be oxidized to hydroxyl radical is +2.27 eV (•OH/H₂O) [31]. while, the oxidation potential of RhB was 0.95 V [32, 33]. Based on the previous energy band analysis of WO₃, it indicated that WO₃ nanoplate and bulk WO₃ both had a powerful enough conduction band for producing O₂^{-•}, but their valence bands were unable to generate •OH. Hence, the photocatalytic mechanism for RhB oxidation over WO₃ was deduced as follows: WO₃ was excited for generation of photo-induced electrons and holes; the electrons were used to reduce the O₂ into O₂^{-•}, which led to the decomposition of RhB, while holes oxidized RhB directly. Moreover, the photocatalytic RhB degradation activity of WO₃ nanoplate did not decrease significantly in 4 cycle tests (Fig. 6D). Additionally, the XRD diffraction patterns of the WO₃ nanoplate after 4 runs reaction (Fig. 6E) did not have obvious variations, indicating that WO₃ nanoplate was a stable photocatalyst for RhB degradation.

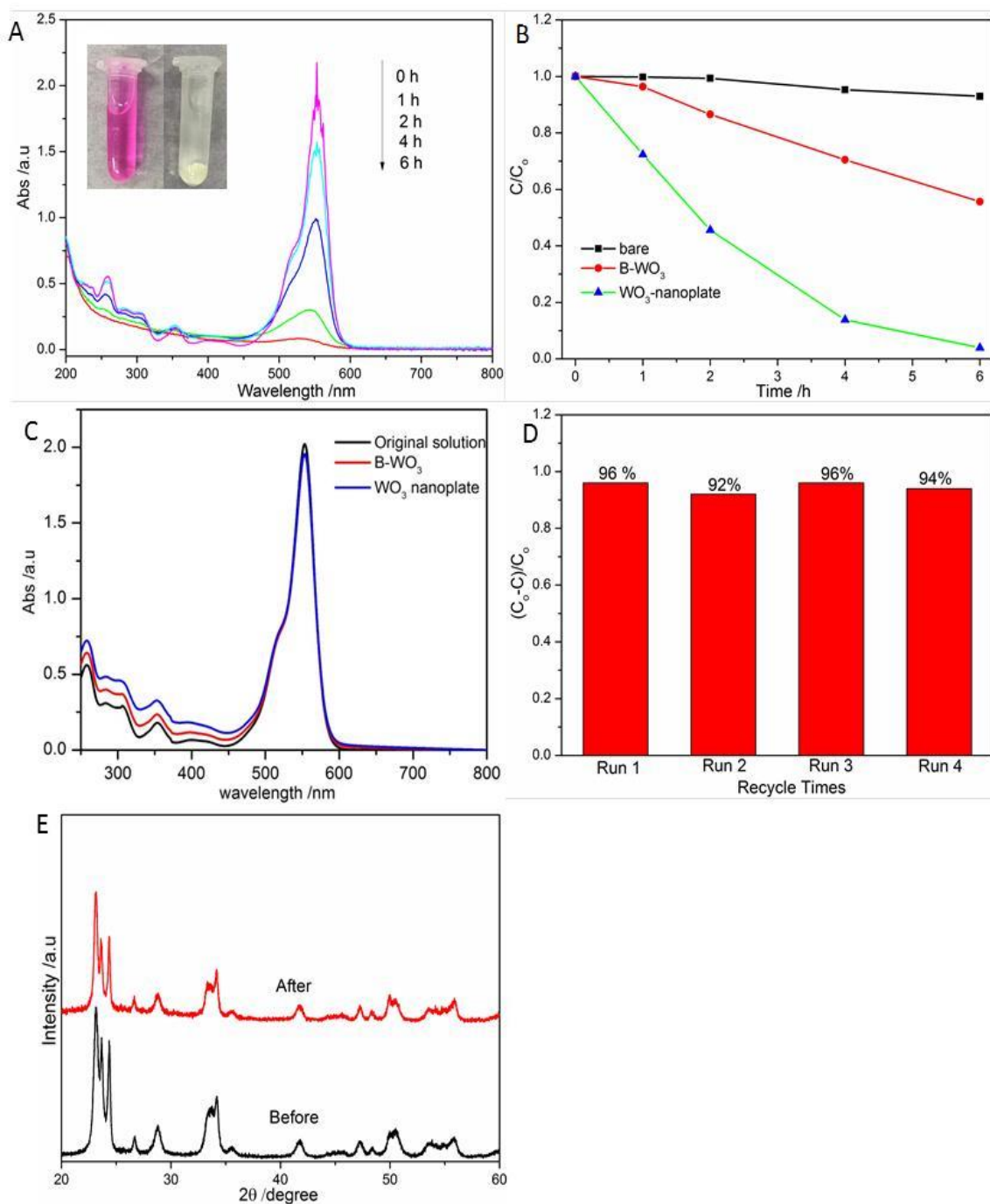


Fig. 6: A) The temporal evolution curve of Uv-vis absorption spectra of RhB aqueous solution over WO_3 nanoplates, inset: RhB solution before (left) and after (right) photocatalytic reaction, B) C/C_0 plotted curve versus time of the samples, C) Uv-vis absorption spectra of RhB before and after adsorption–desorption equilibrium over B- WO_3 and WO_3 nanoplates, D) degradation ratio of recycle tests over WO_3 nanoplates, E) XRD diffraction patterns of the WO_3 nanoplates before and after reaction.

Conclusions

In summary, WO₃ nanoplate were synthesized via a top-down method. XRD and TEM analysis demonstrated WO₃ nanoplate had a monoclinic monocrystal structure. Compared with B-WO₃, WO₃ nanoplate showed an enhanced photocatalytic activity for RhB degradation, about 2.4 times of bulk WO₃. PL spectra, photocurrent and EIS spectra all demonstrated WO₃ nanoplate had a better carrier separation efficacy than B-WO₃, which was ascribed to the main factor for the enhanced photocatalytic activity.

Acknowledgements

National Training Program of Innovation and Entrepreneurship for Undergraduates (202311312011). The authors declare no conflict of interest.

References

- J. Xiong, J. Chen, X. Shao, X. Liu, L. Fu, Insights into the Photosensitive Activity of Monolayer HNb₃O₈ Nanosheets Under Visible Light Irradiation, *Journal of The Chemical Society of Pakistan*, **42**, 807(2020).
- S. Banerjee, S.C. Pillai, P. Falaras, K.E. O'Shea, J.A. Byrne, D.D. Dionysiou, New Insights into the Mechanism of Visible Light Photocatalysis, *The Journal of Physical Chemistry Letters*, **5**, 2543 (2014).
- N. Chankhunthod, P. Junploy, S. Suthirakun, L. Ngamwongwan, C. Phomma, N. Ruchusartsawat, A. Siyasukh, P. Yanu, P. Kijjanapanich, S. Yimklan, A. Rujiwatra, R. Drummond-Brydson, Y. Chimupala, Ecofriendly alkali metal cations diffusion improves fabrication of mixed-phase titania polymorphs on fixed substrate by chemical vapor deposition (CVD) for photocatalytic degradation of azo dye, *Environmental Research*, **239**, 117347 (2023).
- F. Amano, E. Ishinaga, A. Yamakata, Effect of particle size on the photocatalytic activity of WO₃ particles for water oxidation, *The Journal of Physical Chemistry C*, **117**, 22584 (2013).
- K. Villa, S. Murcia-López, T. Andreu, J.R. Morante, Mesoporous WO₃ photocatalyst for the partial oxidation of methane to methanol using electron scavengers, *Applied Catalysis B: Environmental*, **163**, 150 (2015).
- K. Maeda, K. Domen, New Non-Oxide Photocatalysts Designed for Overall Water Splitting under Visible Light, *The Journal of Physical Chemistry C*, **111**, 7851-7861(2007).
- J. Xiong, L. Wen, F. Jiang, Y. Liu, S. Liang, L. Wu, Ultrathin HNb₃O₈ nanosheet: an efficient photocatalyst for the hydrogen production, *Journal of Materials Chemistry A*, **3**, 20627-20632(2015).
- R. Hu, G. Liao, Z. Huang, H. Qiao, H. Liu, Y. Shu, B. Wang, X. Qi, Recent advances of mono-elemental 2D materials for photocatalytic applications, *Journal of Hazardous Materials*, **405**, 124179(2021).
- S. Bai, W. Jiang, Z. Li, Y. Xiong, Surface and Interface Engineering in Photocatalysis, *ChemNanoMat*, **1**, 223-239(2015).
- B. Luo, G. Liu, L. Wang, Recent advances in 2D materials for photocatalysis, *Nanoscale*, **8**, 6904-6920(2016).
- M. Kudo, H. Ohkawa, W. Sugimoto, N. Kumada, Z. Liu, O. Terasaki, Y. Sugahara, A Layered Tungstic Acid H₂WO₇·nH₂O with a Double-Octahedral Sheet Structure: Conversion Process from an Aurivillius Phase Bi₂WO₉ and Structural Characterization, *Inorganic chemistry*, **42**, 4479-4484(2003).
- D. Chen, H. Wang, R. Zhang, L. Gao, Y. Sugahara, A. Yasumori, Single-crystalline tungsten oxide nanoplates, *J. Ceram. Process. Res.*, **9**, 596-600(2008).
- D. Chen, L. Gao, A. Yasumori, K. Kuroda, Y. Sugahara, Size- and shape-controlled conversion of tungstate-based inorganic-organic hybrid belts to WO₃ nanoplates with high specific surface areas, *small*, **4**, 1813-1822(2008).
- S. Limsakul, T. Mahatnirunkul, C. Phomma, T. Chomtong, N. Cholnakasem, S. Yimklan, P. Ruankham, A. Siyasukh, Y. Chimupala, Novel physical sunscreen from one-dimensional TiO₂ nanowire: Synthesis, characterization and the effects of morphologies and particle size for use as a physical sunscreen, *Nano-Structures & Nano-Objects*, **35**, 101027(2023).
- R.E. Schaak, T.E. Mallouk, Exfoliation of layered rutile and perovskite tungstates, *Chemical communications*, 706-707(2002).
- L. Liang, J. Zhang, Y. Zhou, J. Xie, X. Zhang, M. Guan, B. Pan, Y. Xie, High-performance flexible electrochromic device based on facile semiconductor-to-metal transition realized by WO₃·2H₂O ultrathin nanosheets, *Scientific reports*, **3**, 1936(2013).
- M.R. Waller, T.K. Townsend, J. Zhao, E.M. Sabio, R.L. Chamousis, N.D. Browning, F.E. Osterloh, Single-crystal tungsten oxide nanosheets: photochemical water oxidation in the quantum

- confinement regime, *Chemistry of Materials*, **24**, 698-704(2012).
18. J. Yan, T. Wang, G. Wu, W. Dai, N. Guan, L. Li, J. Gong, Tungsten oxide single crystal nanosheets for enhanced multichannel solar light harvesting, *Advanced Materials*, **27**, 1580-1586(2015).
 19. L. Wang, A. Teleki, S.E. Pratsinis, P. Gouma, Ferroelectric WO₃ nanoparticles for acetone selective detection, *Chemistry of Materials*, **20**, 4794-4796(2008).
 20. D. Chen, Y. Sugahara, Tungstate-based inorganic-organic hybrid nanobelts/nanotubes with lamellar mesostructures: Synthesis, characterization, and formation mechanism, *Chemistry of Materials*, **19**, 1808-1815(2007).
 21. X. Chen, Y. Zhou, Q. Liu, Z. Li, J. Liu, Z. Zou, Ultrathin, single-crystal WO₃ nanosheets by two-dimensional oriented attachment toward enhanced photocatalytic reduction of CO₂ into hydrocarbon fuels under visible light, *ACS applied materials & interfaces*, **4**, 3372-3377(2012).
 22. J. Xiong, K. Jing, J. Zou, S. Liang, L. Wu, A hybrid of CdS/HCa₂Nb₃O₁₀ ultrathin nanosheets for promoting photocatalytic hydrogen evolution, *Dalton Transactions*, **46**, 13935-13942(2017).
 23. A. Somdee, S. Wannapop, Enhanced photocatalytic behavior of ZnO nanorods decorated with a Au, ZnWO₄, and Au/ZnWO₄ composite: Synthesis and characterization, *Colloid and Interface Science Communications*, **47**, 100591(2022).
 24. Y. Zang, L. Li, Y. Zuo, H. Lin, G. Li, X. Guan, Facile synthesis of composite g-C₃N₄/WO₃: a nontoxic photocatalyst with excellent catalytic activity under visible light, *RSC Advances*, **3**, 13646-13650(2013).
 25. X. She, J. Wu, J. Zhong, H. Xu, Y. Yang, R. Vajtai, J. Lou, Y. Liu, D. Du, H. Li, P.M. Ajayan, Oxygenated monolayer carbon nitride for excellent photocatalytic hydrogen evolution and external quantum efficiency, *Nano Energy*, **27**, 138-146(2016).
 26. Q. Li, Q. Tang, P. Xiong, D. Chen, J. Chen, Z. Wu, H. Wang, Effect of palladium chemical states on CO₂ photocatalytic reduction over g-C₃N₄: Distinct role of single-atomic state in boosting CH₄ production, *Chinese Journal of Catalysis*, **46**, 177-190(2023).
 27. S. Wannapop, A. Somdee, Highly orientated one-dimensional Cu₂O/TiO₂ heterostructure thin film for photoelectrochemical photoanode and photocatalytic degradation applications, *Thin Solid Films*, **747**, 139144(2022).
 28. Z. Chen, D. Li, W. Zhang, Y. Shao, T. Chen, M. Sun, X. Fu, Photocatalytic Degradation of Dyes by ZnIn₂S₄ Microspheres under Visible Light Irradiation, *The Journal of Physical Chemistry C*, **113**, 4433-4440(2009).
 29. M. Sun, D. Li, Y. Chen, W. Chen, W. Li, Y. He, X. Fu, Synthesis and Photocatalytic Activity of Calcium Antimony Oxide Hydroxide for the Degradation of Dyes in Water, *The Journal of Physical Chemistry C*, **113**, 13825-13831(2009).
 30. X. Hu, T. Mohamood, W. Ma, C. Chen, J. Zhao, Oxidative Decomposition of Rhodamine B Dye in the Presence of VO₂⁺ and/or Pt(IV) under Visible Light Irradiation: N-Deethylation, Chromophore Cleavage, and Mineralization, *The Journal of Physical Chemistry B*, **110**, 26012-26018(2006).
 31. S.G. Kumar, L.G. Devi, Review on modified TiO₂ photocatalysis under UV/visible light: selected results and related mechanisms on interfacial charge carrier transfer dynamics, *The Journal of physical chemistry A*, **115**, 13211-13241(2011).
 32. Z. Xiong, L.L. Zhang, J. Ma, X.S. Zhao, Photocatalytic degradation of dyes over graphene-gold nanocomposites under visible light irradiation, *Chemical Communications*, **46**, 6099-6101(2010).
 33. T. Shen, Z.-G. Zhao, Q. Yu, H.-J. Xu, Photosensitized reduction of benzil by heteroatom-containing anthracene dyes, *Journal of Photochemistry and Photobiology A: Chemistry*, **47**, 203-212(1989).